

Flooded by Success: On the role of electrode wettability in CO₂ electrolyzers that generate liquid products

McLain E. Leonard¹, Michael J. Orella¹, Nicholas Aiello¹, Yuriy Román-Leshkov¹,

Antoni Forner-Cuenca^{1,2}, and Fikile R. Brushett^{1,z}

¹ Department of Chemical Engineering, Massachusetts Institute of Technology, Cambridge, MA, 02139, USA

² Membrane Materials and Processes, Department of Chemical Engineering and Chemistry, Eindhoven University of Technology, Het Kranenveld 14, P.O. Box 513, 5600 MB Eindhoven, The Netherlands

^z E-mail: brushett@mit.edu, Phone: 617-324-7400

KEYWORDS: wettability, flooding, gas diffusion electrode, electrochemical reduction, carbon dioxide, organic products

ORCID:

McLain E. Leonard: [0000-0003-4572-5251](https://orcid.org/0000-0003-4572-5251)

Michael J. Orella: [0000-0003-1207-4704](https://orcid.org/0000-0003-1207-4704)

Nicholas Aiello: [0000-0002-7507-6937](https://orcid.org/0000-0002-7507-6937)

Yuriy Román-Leshkov: [0000-0002-0025-4233](https://orcid.org/0000-0002-0025-4233)

Antoni Forner-Cuenca: [0000-0002-7681-0435](https://orcid.org/0000-0002-7681-0435)

Fikile R. Brushett: [0000-0002-7361-6637](https://orcid.org/0000-0002-7361-6637)

Abstract

Economic operation of carbon dioxide (CO_2) electrolyzers generating liquid products will likely require high reactant conversions and product concentrations, conditions anticipated to challenge existing gas diffusion electrodes (GDEs). Notably, electrode wettability will increase as lower surface tension products (e.g., formic acid, methanol, ethanol, and 1-propanol) are introduced into electrolyte streams potentially leading to flooding. To understand the hydraulically stable electrolyzer operating envelopes in mixed aqueous-organic liquid domains, we connect intrinsic electrode wettability descriptors to operating parameters such as electrolyte flow rate and current. We first measure contact angles of water-organic dilutions on polytetrafluoroethylene (PTFE) and graphite surfaces as planar analogues for GDE components. We then use material balances around the reactive gas-liquid interface to calculate product mass fractions as functions of water sweep rate and current. Product composition maps visualize the extent to which changes in cell performance influence capillary pressure, a determinant of GDE saturation. Analyses reveal that formic acid mixtures pose little risk for GDE flooding across a wide range of sweep-rate/current combinations, but effluents enriched with less than 30% alcohol by mass may cause flooding. This study indicates opportunities to integrate oleophobic surface treatments that repel aqueous and organic liquids into GDEs to expand stable operating regions.

Introduction

Electrochemical carbon dioxide reduction (CO₂R) is increasingly recognized as a viable technology for flexible generation of chemicals using carbon dioxide (CO₂) recovered from industrial exhaust streams or directly captured from air.^{1,2} When coupled with affordable electricity generated from renewable sources, CO₂R has the potential to displace petroleum-based chemicals production in a low-carbon economy.³ Given that the form factors of electrochemical technologies evolve as they transition from benchtop prototypes in the laboratory to engineered unit operations integrated into an industrial process, it is reasonable to anticipate commensurate shifts in the objectives and challenges for each scale. Historically, three-electrode analytical cells have been used to study catalyst activity, selectivity, and stability with a goal of incorporating proven materials into larger devices.⁴⁻⁶ However, it has been recognized that the limited CO₂ flux through bulk volumes of liquid electrolyte suppress the reaction rate of CO₂ and inhibit the performance of otherwise promising catalyst systems.⁷⁻⁹ Gas fed electrolyzers adapted from commercially successful water electrolyzer and fuel cell technologies have motivated CO₂R researchers to explore various combinations of porous electrodes, catalyst layers, liquid electrolytes, and membranes to achieve higher areal productivity while maintaining steady fluxes of species between flow channels and the active sites.¹⁰⁻¹⁴ For example, present art demonstrates that high current density production (> 200 mA cm⁻²) of valuable intermediates, such as carbon monoxide (CO), at moderate cell voltages (ca. 3 V) and relatively extensive durations (> 100 h) is achievable at ambient conditions using cell configurations similar to polymer electrolyte water electrolyzers.¹⁵

Such impressive demonstrations of this technology beg the question: could success in operating electrolyzers towards high product generation rates result in reaction environments so extreme that they challenge the stability limits of existing porous electrode materials sets? We posit that the conditions necessary for industrial CO₂R may render GDEs composed of hydrophobic materials incompatible with lower-surface-tension mixed aqueous-organic phases generated from the reactive gas-liquid interface. In this work, we consider the wettability of GDE components, evinced by the sessile drop contact angle on planar analogues, in contact with aqueous-organic liquid mixtures representative of potential product stream compositions. Subsequently, we use a simple mass balance model paired with contact angle measurements to estimate electrolyzer operating limits, represented by the capillary pressure, beyond which product streams would be anticipated to spontaneously flood conventional GDEs without deploying additional pressure control strategies. By connecting readily obtainable measures of electrode-liquid affinity to cell operating conditions, we aim to develop insights into operating regimes for CO₂ electrolyzers that generate liquid products and to address critical questions such as: (i) Do target effluent compositions fall within stable region for PTFE-based GDEs? (ii) What are threshold compositions for liquid product mixtures that may lead to spontaneous electrode wetting under pressure-balanced conditions? (iii) Can we design porous electrodes

with flooding resilient structures and surface functionalities to withstand high product concentrations?

Industrial CO₂ to liquids electrolyzers will move beyond differential operation

At the bench-scale, where component validation and performance benchmarking are typically the desired outcomes, electrochemical cells with active areas of ca. 1–10 cm² are often operated to generate dilute product streams that are conducive to quantitative analyses. By operating electrolyzers under differential conditions, in which species concentrations gradients are assumed to be negligible,¹⁶ electrochemical kinetic parameters can be determined in the absence of mass transfer limitations that may obscure results at higher degrees of reactant depletion. When targeting gas-phase products, such as CO, differential conditions are generally achieved by feeding CO₂ in stoichiometric excess to the cathode compartment to ensure low single-pass CO₂ conversion (< 20%) (**Figure S1**, Supplementary Information) for a given total current. For cells with flowing electrolytes, water-miscible liquid products can be diluted either by increasing the total electrolyte volume for batch operation or increasing flow rate in single-pass operation. As an added benefit, generating dilute products can reduce the risk of creating dangerous concentrations and/or quantities of hazardous reaction products that are more appropriately handled in industrial settings where suitable hazard management protocols exist.

In contrast, the choice of operating conditions and reactor architecture for commercial CO₂R systems will be driven by application economics to the point that the set of idealized scenarios explored at the bench-scale may not reflect practical device set points. Indeed, it may be more cost-effective to operate electrolyzers so that both gaseous and liquid effluents are highly enriched in CO₂R products. Results from our previously reported general technoeconomic model indicate that separations could constitute a larger fraction of overall CO₂R process cost when generating liquid products as opposed to gaseous products.¹⁷ Based on this coarse analysis, we can predict that process economics, driven by the desire to minimize downstream separations of liquid products from the carrier phase, will likely dictate that future at-scale CO₂R systems generate higher product concentrations than those contemplated at the laboratory-scale today. However, operating in this manner, in turn, may give rise to scientific and engineering challenges that, to date, remain unarticulated. Accordingly, publications focused on scale-up have begun to highlight electrolyzers which operate with high current densities,¹⁸ large total currents,¹⁹ and, to a lesser extent, enriched product streams.^{20–22}

As CO₂R cell prototypes begin to traverse these new operating regimes, challenges can be anticipated due to shifts in chemical compatibility requirements for reactor components (catalysts, electrodes, periphery), significant deviations from low-concentration kinetic behavior, and greater process safety concerns arising from concentrated toxic products. Here, we elect to focus on irregularities expected to arise for gas diffusion electrodes (GDEs) while operating gas-fed CO₂R devices at high liquid product generation rates as the other topics are

more widely studied at present. Recent reports of flowing electrolyte CO₂R cells with extended durability (ca. 10–100 h) have generally espoused the importance of incorporating fluorinated polymers (i.e., polytetrafluoroethylene (PTFE)) in the GDEs, either as an additive or a structural component, to maintain a stable gas-liquid interface between the liquid product/electrolyte phase and gaseous reactant phase.^{18,23,24} This idea has credence given historical uses of fluorinated polymers such as PTFE and fluorinated ethylene propylene (FEP) as *hydro-phobic* coatings for carbon fiber gas diffusion layers to assist in water management in fuel cell operations²⁵ or as components in oxygen depolarized GDEs for their capacity to aid in facile oxygen reduction by maintaining stable gas-electrolyte interfaces.²⁶ Indeed, initial investigations by Haas *et al.* and Dinh *et al.* would suggest that fluoropolymer-rich GDEs can significantly improve operating lifetimes of a variety of CO₂R cell architectures.^{24,27} While PTFE as a GDE support has expanded the envelope for high-current electrolysis, stability at the cathode-electrolyte interface is expected to be perturbed by high concentrations of liquid products such as alcohols, which have also been reported to dissolve anion-exchange membrane materials *in situ*.²¹

Gas diffusion electrode flooding is governed by capillary pressure and wettability

In CO₂R, the GDE serves as (i) a scaffold for the catalyst layer and (ii) an interface between the gaseous and liquid phases that facilitates flux of reactants/products/electrons to/from the catalytically active sites. A key challenge is the rational selection of GDE materials that can balance both primary (e.g., electrical conductivity and electrocatalytic activity/selectivity) and secondary (e.g., permeability and chemical compatibility) functionalities across a range of operating modes. Crucially, the stability of the cathode-electrolyte interface is intimately tied to the *wettability* of the GDE, that is captured by the value of the solid-liquid-gas contact angle, θ . Importantly, this angle can define the sign of the equilibrium trans-interfacial pressure difference between two immiscible phases in a porous medium. If we consider an idealized porous medium to be composed of cylindrical pores, or capillaries, we can use **Equation 1**, as proposed by Washburn,²⁸ to calculate the capillary pressure, P_C , as a function of the contact angle, θ , the pore radius, r , and the liquid-gas surface tension, γ . Crucially, P_C defines the difference at equilibrium between the gas and liquid phase pressures (P_G , P_L).²⁹

$$P_C = P_L - P_G = \frac{-2\gamma \cos \theta}{r} \quad \text{Equation 1}$$

Although this simple model for capillary pressure may not completely capture the behavior of real porous materials due to effects including tortuosity, constrictions, and dead ends, the relationships between parameters evinced by **Equation 1** remain generally valid.

Understanding the effects of material selections on wettability properties of the electrodes requires a comprehension of surface energetics. Electrodes are often combinations of high

energy (HE; metal or carbon) materials that readily wet most liquids³⁰ and low energy (LE; binders or additives) materials used to wet-proof the surfaces. Modifications to electrode surfaces can drastically change wettability characteristics regardless of the bulk material.³⁰ In the 1960's, pioneering work by Zisman characterized the spreading and adhesion of liquids on solids as a function of surface energy/surface tension.³¹ Evidently in the context of fluid droplets on planar solids, the (i) macroscopic solid-liquid-gas contact angles track with the composition of test fluids according to the surface tension and (ii) test fluids transition from non-wetting ($\theta > 0^\circ$) to wetting ($\theta = 0^\circ$) on a given solid at a surface energy (surface tension) threshold value that depends on the chemical character and physical structure of the surface.

Commonly pursued CO₂R products like organic acids (i.e., formic acid) and C1–C3 primary alcohols (i.e., methanol, ethanol, 1-propanol) are water-miscible at ambient conditions, so even at dilute concentrations, these species can greatly affect physical properties such as density, viscosity, and liquid-gas surface tension (**Figure S2**). Changes to density and viscosity affect pressure drops within flowing electrolyte-based cells; however, we choose not to focus on pumping duties in this work. Changes to surface tension/contact angle, in combination with electrode geometries, most directly influence GDE wetting and saturation, which acutely impact reactant fluxes and, therefore, electrocatalytic performance. Surface tension in electrolyte solutions can be influenced by a many factors including ionic strength, anion-cation pair, and temperature.^{32–36} Given the breadth of the compositional space and potential testing conditions, here we elect to focus on the introduction of organic components into solution because they are anticipated to most drastically impact surface tension. Further analyses may explore how these effects are amplified or suppressed depending on electrolyte composition or operating conditions.

Measuring the *apparent* contact angles of sessile droplets is an effective method for characterizing the wettability of candidate porous electrode materials with a variety of test liquids reminiscent of CO₂R product streams. Although this macroscopic approach is often applied to study non-ideal substrates, *intrinsic* contact angles can only be measured on smooth, non-porous surfaces (Young's theory).³⁷ Appropriate corrections to contact angles measured on textured materials, which appear distorted when compared to flat materials with equivalent surface chemistry,³⁰ can be made for both homogenous (Wenzel) and heterogeneous (Cassie-Baxter) wetting regimes.^{38,39} Despite the obscurations introduced by roughness and entrapped fluids when determining quantitative measures of wettability on porous substrates, droplet based-protocols are widely practiced to qualitatively evaluate the resistance of textiles and other functional materials to wetting.^{40,41}

Experimental

Contact angle measurements with sessile drop goniometry

To better understand the wettability of aqueous-organic mixtures in the context of CO₂R,

we selected formic acid (FA; reagent grade, $\geq 95\%$ purity, Sigma-Aldrich), methanol (MeOH; HPLC grade, $\geq 99.9\%$, Sigma-Aldrich), ethanol (EtOH; anhydrous, 200 Proof, KOPTEC), and 1-propanol (PrOH; ACS reagent, $\geq 99.5\%$) for analysis. We prepared solutions across a range of dilutions from 0 to 100% by mass with deionized (DI) water (18.2 M Ω , Milli-Q). Salt-free solutions were used to isolate the interaction between each test liquid and water. Subsequent studies may contemplate the impacts of the chemistry and concentration of dissolved salts on relevant physical properties. FA mixtures were used in place of formate salt solutions because this study focuses on the effect of introducing organic solvent components into aqueous solutions. Although formate salt product mixtures are more typically reported in the literature, some high productivity electrolyzers utilizing porous solid electrolytes can generate salt-free, concentrated acid product streams, making a focus on FA applicable.^{20,42} Additionally, organic acid solutions are known to have lower surface tension than electrolyte solutions, so FA has utility when used for a bounding study focused on negative surface tension deviations from water.^{33,34} PTFE (FP303050, Goodfellow) and graphite (99.997%, 867-421-20, Goodfellow) sheets were used as the primary solid substrates for droplet studies. PTFE sheets were cleaned with DI water and isopropyl alcohol (IPA) and dried using compressed air prior to analysis. Graphite sheets were prepared by removing the top layer of material with Scotch® tape (MFR#: 810, 3M). 5- μ L droplets were dispensed onto substrates using an automatic pipetting unit. Measurements were taken in ambient air where the temperature and relative humidity remained between 20–24 °C and 10–40%, respectively. Videos of 30–60 second duration were captured using a contact angle goniometer system (Model 200, ramé-hart) and processed using DropPy V1.0.0a0, a Python-based goniometer software.⁴³ Substrates were spot-cleaned before dispensing and imaging new droplets. Contact angles were determined by fitting edges with a two-parameter Bashforth-Adams model that accounts for the effects of gravity on droplet shape. Additional descriptions of experimental procedures (**Sections S.1** and **S.2**) as well as the data collected for each trial (**Tables S1** and **S2**) are provided in the Supplementary Information.

Contact angle measurements with select CO₂R products as test liquids

To determine the qualitative impact of mixed organic-aqueous product streams on electrode wettability, we measured the contact angles for the solutions described above as a function of water content, as shown in **Figure 1**. The markers for each product represent the average contact angle from 5 trials at each concentration and the error bars are one standard deviation of the same measurements. As expected, the contact angles of the mixtures on both surfaces decrease with increasing mass fraction of organic species due to the reducing surface tension. The tendency to wet the solids is directly proportional to the carbon chain length of the product which is associated with decreased polarity and surface tension (PrOH < EtOH < MeOH < FA < water), especially for the primary alcohols.⁴⁴ The ability for each solid to prevent wetting can be studied, at a high level, by comparing the point at which the test fluid

is neutrally wetting, e.g., has a contact angle of 90° . When studying graphite, fluids with more than 10% alcohol fall below the 90° -threshold; however, the alcohols can be mixed in higher proportions before neutrally wetting conditions are reached on PTFE. In both cases, the formic acid mixtures reach neutrally wetting conditions at much greater mass fractions than the alcohols, suggesting that such product streams will not lead to significant changes in capillarity relative to pure aqueous solutions in PTFE-based GDEs. As such, CO₂R to FA appears to have a wide range of feasible operating compositions, exceeding the highest reported concentrations to date (ca. 15% by mass).²⁰ In contrast, the alcohol crossover concentrations are significantly lower and we anticipate that such compositions will be readily-achievable in practical CO₂ to liquid electrochemical processes posing a stability challenge for PTFE-based GDEs.

Beyond experimental measurements of the apparent contact angles of test fluids, γ can be used as a common predictor for the wettability of different fluid mixtures.³⁰ With the previous θ measurements, we can construct Zisman plots (**Figure 2**) to predict the critical surface tension, γ_{C0} , for complete wetting ($\theta = 0^\circ$) and the surface tension at the crossover composition, γ_{C90} , ($\theta = 90^\circ$) for both graphite (**Figure 2a**) and PTFE (**Figure 2b**). We fit the data (black open circles) for each surface with quadratic functions (red lines), which is reasonable based on previous analyses that used similar empirical fits.³¹ We then predict γ_{C0} values of 34.8 mN/m for graphite (RMSE = 4.1 mN/m) and 21.9 mN/m for PTFE (RMSE = 2.4 mN/m). We validated this method using a secondary set of test fluids and determined γ_{C0} to be 14.8 mN/m for PTFE. The validation data (**Table S3**) along with an additional Zisman plot (**Figure S3**) can be found in the Supplementary Information. As can be seen for graphite, the data below 31.8 mN/m represent the product compositions that completely spread when contacting the solid. Note that none of the dilutions tested were of sufficiently low surface tensions to reach the critical point for PTFE, so the empirical fit is needed to estimate γ_{C0} . The γ_{C90} for graphite and PTFE are predicted to be 45.2 mN/m and 47.2 mN/m, respectively. These values are useful for predicting sign changes in P_c , as will be considered in the next section. For comparison, Zisman reported a γ_{C90} of ca. 40 mN/m for PTFE, but did not report a value for graphite, which is reasonable given the wettability of graphite surfaces vary widely depending on form factor.⁴⁵ Indeed, identification of smooth, flat material as a representative proxy for carbon particles and/or fibers remains elusive. Qualitatively, the γ_{C0} value predicted for graphite exceeds that of PTFE, which is to be expected as it is the higher energy material.

Operating envelopes are mapped using electrolysis mass balances

Model formulation

While *ex situ* contact angle data only provide qualitative insights on wettability for porous electrodes, such understanding informs materials selection for different classes of reactions. Here, we use wettability data in combination with a simple mass balance model around the cathode reaction zone to estimate ranges of feasible operating conditions before liquid product

enrichment near the gas-liquid interface leads to electrode flooding. A mass balance model represented by the schematic in **Figure 3** accounts for the mass flow rates of water and organic products to/from a well-mixed flowing liquid phase control volume. The results and possible implications of changing electrolyzer set points are discussed in the context of the widely studied flowing liquid electrolyte configuration.^{8,10,23,24,27,46–58} In lieu of using flowing electrolytes, some recently reported bench-scale CO₂R electrolyzers instead integrate dense polymer electrolyte membranes,²¹ porous polymer electrolytes,⁴² or ionomer-coated packed beads²⁰ to decouple ion flow from product collection and removal in order to generate salt-free aqueous-organic mixtures. Although inspired by cells which use a flowing electrolyte format, the zero-dimensional mass balance approach serves to bound the operating space of CO₂R systems without assuming device-specific geometry. It should also be noted that this model cannot predict location-specific flooding susceptibility based on operating conditions and cell geometry.

Faraday’s law of electrolysis connects the mass flow rates for product generation, $\dot{m}_{P,rxn}$, (**Equation 2**) and water consumption, $\dot{m}_{W,rxn}$, (**Equation 3**) at the cathode to the current (I) and one of the two stoichiometric constants, z_P and z_W , which correspond to the number of electrons per mole of product generated and water consumed, respectively.

$$\dot{m}_{P,rxn} = \frac{I}{z_P F} M_P \quad \text{Equation 2}$$

$$\dot{m}_{W,rxn} = \frac{I}{z_W F} M_W \quad \text{Equation 3}$$

In these equations, F is the Faraday constant ($96485 \text{ C mol e}^{-1}$), M_P is the molar mass (kg/mol) of a product species, and M_W is the molar mass of water. The mass flow rate of feed water, $\dot{m}_{W,in}$, is defined (**Equation 4**) as a function of the inlet volumetric sweep rate, Q , and the density of water, ρ_W .

$$\dot{m}_{W,in} = \rho_W Q \quad \text{Equation 4}$$

Generally, the *sweep rate* of liquid electrolyte impacts product flux away from the catalyst layer to the bulk electrolyte and, by extension, the distribution of product concentrations along the reactor length and at the exit. In this treatment, we select Q directly to regulate product dilution for a given current, but this ability to independently control product removal and tune dilution would be hampered in polymer-electrolyte-based devices as alternative flux mechanisms like evaporation and membrane crossover are less readily controlled.²¹

We implement material balances around electrons, water, and liquid reaction products to directly calculate the total mass flow rate exiting the reactor, \dot{m}_{out} (**Equation 5**), while ignoring dissolved gases (e.g., CO₂, hydrogen, carbon monoxide, etc.) and dissociated ions such as hydroxide (OH[−]) produced from the cathodic half-reactions as well as bicarbonate (HCO₃[−])

and carbonate (CO_3^{2-}) that form as a result of carbonation reactions.⁵⁹ We also choose to set the product feed rate, $\dot{m}_{\text{P,in}}$, to zero in this study.

$$\dot{m}_{\text{out}} = (\dot{m}_{\text{W,in}} - \dot{m}_{\text{W,rxn}}) + (\dot{m}_{\text{P,in}} + \dot{m}_{\text{P,rxn}}) \quad \text{Equation 5}$$

Through substitution, we define the product mass fraction, x_{P} (**Equation 6**), as the total product mass divided by the total mass exiting the reaction zone as a function of total current, I , and inlet water volumetric sweep rate, Q .

$$x_{\text{P}} = \frac{\dot{m}_{\text{P,in}} + \dot{m}_{\text{P,rxn}}}{\dot{m}_{\text{out}}} = \frac{\dot{m}_{\text{P,in}} + \frac{I}{z_{\text{P}}F} M_{\text{P}}}{\left(\rho_{\text{W}} Q - \frac{I}{z_{\text{W}}F} M_{\text{W}} \right) + \left(\dot{m}_{\text{P,in}} + \frac{I}{z_{\text{P}}F} M_{\text{P}} \right)} \quad \text{Equation 6}$$

Here, I can either represent a partial current towards a target product or, assuming 100% faradaic efficiency, a total current. The water mass fraction, x_{W} (**Equation 7**), is readily determined from x_{P} because we assume a binary mixture in the liquid phase.

$$x_{\text{W}} = 1 - x_{\text{P}} \quad \text{Equation 7}$$

Each cathodic half reaction consumes CO_2 , H_2O , and electrons and produces hydrogenated products and OH^- as shown in **Table 1**. Included are the relevant stoichiometric constants— n_{P} (the number of moles of CO_2 per mole of product), z_{P} , and z_{W} —as well as M_{P} for each product. We convert from a mole to mass basis because it can be more convenient to work with mass (or weight) fractions at high solute concentrations.

This simple mass balance analysis enables consideration of the cumulative impact of water consumption and organic product generation on the physical properties of the solution and the wettability of the electrode. Note that the stoichiometric constants used in this model only account for the water consumption in cathode half-reactions, as the microenvironment local to the electrode-electrolyte interface will determine flooding. However, it should be noted that in a full cell water is generated at the anode during the oxygen evolution reaction. Depending on the cathode reaction stoichiometry, this source could offset some or all the water consumption (**Table S4**, Supplementary Information). For example, there is no net water consumed for the conversion of CO_2 to formate/FA, but CO_2 to alcohols reactions still result in net water consumption. By focusing on the cathode water consumption, this model serves to construct a conservative upper bound for organic product concentrations that could be anticipated for a given chemistry, current, and liquid sweep rate.

Model results and discussion

We construct composition contour plots for FA, MeOH, EtOH, and PrOH (**Figure 4**) by calculating x_{P} across many currents and flow rates. The y-axes are reported on a log scale for clarity across several magnitudes of flow rates. Composition isoclines reported in product content mass (%), solid lines) start at the 0.1, 1, and 10% and then continue from 10–100% in

increments of 10%. Sweeping the current from 0–1000 mA at fixed Q results in a linear increase in the production rate (**Equation 2**), while increasing Q from 0.001–1 mL min⁻¹ at fixed I decreases x_P due to their inverse relation. The composition contours generally shift downward with deeper reduction products and increasing molar mass, with an exception of FA that has similar molar mass to EtOH. FA composition is less sensitive to Q at fixed I , whereas the alcohols are more likely to reach high concentration through modest changes to Q .

Determining 90°-crossover compositions from *ex situ* contact angle data allows us to estimate a band of operating conditions that may lead to an unfavorable P_C sign change (i.e., from positive to negative). We use wettability metrics for PTFE to represent GDE stability because it is assumed to be invariant to mild voltage biases within the electrode. In contrast, graphite is the more polarizable GDE component, so we may anticipate that its wettability will increase as a function of electrode voltage according to electrowetting phenomena.^{60,61} The measured crossover composition, here, corresponding to a measured 90° contact angle on PTFE, is indicated with a black dot-dash line for each of the product subpanels in **Figure 4**. These crossover compositions were determined by interpolating between measured data points (**Figure S4**, Supplementary Information). If making predictions using a Zisman rule, all liquids with γ below that of a crossover value, which is either 47 mN/m (\cdots , this work) or 40 mN/m ($--$, Zisman), should wet PTFE with a contact angle less than 90°. We estimate the crossover composition for each CO₂R product by finding the water composition at which the γ curves (**Figure S2b**, Supplementary Information) reach the 90°-threshold. While there are discrepancies between the measurements and predicted isoclines, the differences between the operating conditions needed to achieve each composition are relatively minor. At flow rates above each crossover line, the sweep stream provides enough water to the reaction zone at a given current to keep the product composition below the critical imbibition point. Put another way, for a given sweep rate, the electrochemical conversion rate is slow enough that enrichment of organic species in the reaction zone is not so great as to lead to flooding.

In agreement with the contact angle measurements, the ordering and position of the crossover composition isoclines in Q - I space align with the γ and polarity of the organic species (**Figure S2b**, Supplementary Information). Plotting the isoclines for different liquid species together (**Figure 5**) is an effective way for determining if electrolyzer operating conditions need to be tailored according to product identity. For example, although FA mixtures reach the crossover point at much high concentrations as compared to the alcohol mixtures, the operating conditions required to reach zero capillary pressure are similar for species of equivalent polarity. At the extremes of species wettability (i.e., PrOH versus FA), however, the Q required to induce contact angle crossover varies by nearly an order of magnitude at the same I .

Now with x_P mapped to different operating conditions, we can connect the wettability of the various liquid mixtures to a simple prediction of equilibrium P_C using **Equation 1**, which is helpful for understanding the pressure differentials required to maintain a stable gas-liquid

interface in a gas fed CO₂ electrolyzer. Again, here we do not initially consider complex physical and geometric features evident in real GDE materials (thickness, pore size distribution, fibers spacing, particles sizes, mixed wettability)^{62,63} to determine P_C or flooding dynamics because simplified models suffice for capturing general capillarity trends. However, further analyses explicitly considering saturation or wetting dynamics in electrodes with finite volume could expand from these zeroth-order analyses of interfacial P_C to refine predictions of stable operating envelopes.

Next, we compute P_C at various levels of water content, x_w (**Figure 6**) in order to translate product composition to equilibrium interfacial pressure along the contours in **Figure 4**. The P_C data associated with this figure are reported in **Table S5** in the Supplementary Information. We employ interpolated PTFE contact angle values (**Figure S4**) to calculate P_C with a radius, r , of 15 μm as representative of the effective pore radius for gas diffusion layers.⁶³ If we were to overlay the P_C onto the corresponding composition contours of **Figure 4**, these new isoclines would serve to approximate the magnitude of the maximum liquid-gas overpressure that a GDE could withstand while still maintaining interfacial stability/avoiding flooding. This approach allows for the insertion of P_C models that are uniquely suited to specific electrode microstructure and surface functionalization. Comparing the operating envelope for each liquid-PTFE combination as a function of current and flow rate is useful for predicting if any notable physical changes to the system pressure equilibrium emerge when targeting different CO₂R products. The critical composition lines generally shift upward from FA to PrOH, according to chain length, depth of electroreduction, and decreasing polarity, which taken together indicate that the allowable operating space will narrow as the deeper CO₂R products considered in this subset are pursued.

These results suggest that the operating envelope for FA is likely to be wider than for alcohols for PTFE-supported GDEs. However, when considering that many existing industrial GDEs are composite materials (conductive metal and hydrophobic PTFE components) with mixed wettability properties (*vide supra*, oxygen depolarized cathodes), these contours may constitute the an *optimistic* set of conditions correlating to P_C crossover. Using composite GDEs may ultimately prove necessary when scaling to larger cell areas due to enhanced through-plane conductivity as compared to the PTFE-supported electrodes. Despite the increased flooding risk imparted to GDEs by imbuing them with conductive additives, there are still opportunities for targeted tuning wet-proofing content in porous media to achieve both favorable P_C envelopes⁶⁴ as well as high CO₂R activity and faradaic efficiency.^{8,52}

This mass balance analysis serves to estimate P_C thresholds for porous electrodes in contact with low-surface tension liquid mixtures. However, what is not evident from the analysis until now is that pore geometry and surface wettability *together* determine P_C in real porous media. Therefore, in the next two sections we briefly discuss the potential for leveraging porous media microstructure and novel surface chemistry modifications to engineer more

robust porous electrodes for CO₂ to liquids electrolyzers.

Opportunities for selecting electrode microstructure to prevent spontaneous flooding

Using idealized cylindrical pore geometry alone to determine electrode stability thresholds might lead us to predict that liquid mixtures spontaneously enter porous media precisely at the 90° crossover point. However, porous electrodes often consist of non-ideal material geometries, such as packed particles or entangled fibers, that can exhibit non-intuitive imbibition behavior.⁶² Inspired by the earlier work of Purcell⁶² and Mason & Morrow⁶⁵, Forner and co-workers developed a constricted pore model and used it, in part, to explain why patterned hydrophilic channels in fibrous gas diffusion media did not spontaneously fill with water.⁶³ This adaptation of the Washburn model framework shown in **Equation 8** appears similar to **Equation 1**, but allows for a variable pore radius, $r = r(z)$, and introduces a new variable called the filling angle, $\alpha = \arctan(dr/dz)$, which changes according the local derivative of the pore profile.

$$P_C = P_L - P_G = \frac{-2\gamma \cos(\alpha + \theta)}{r} \quad \text{Equation 8}$$

It is important to note that $P_C = P_C(z)$ since the pore diameter varies according to the longitudinal position along the pore channel. Therefore, the operable output of this model is the *maximum capillary pressure* along the channel length, since the location of highest resistance determines whether the liquid will advance into, or flood, the pore. For this analysis, we use a maximum pore diameter, d_{\max} , of 30 μm , and fiber diameter of 20 μm as representative of fuel cell gas diffusion layers. A schematic of the pore geometry (**Figure S5**) along with more details about the modified capillary pressure expression (**Section S.3**) and the model's parameter sensitivities (**Figures S6–S8**) are provided in the Supplementary Information.

Exploring the resistive effect imparted by α , we calculate the maximum P_C as a function of the constriction aspect ratio, d_{\min}/d_{\max} , or the ratio between minimum and maximum pore diameters. Each contour in **Figure 7** corresponds to a generic CO₂R liquid aqueous-organic mixture in contact with PTFE surface. The surface tension and PTFE contact angle combinations (γ, θ) for each contour are functionally defined by the polynomial fit shown in **Figure 2b**. The results reported in this plot indicate that, as might be expected, solutions with $\theta_{\text{PTFE}} > 90^\circ$ have a maximum $P_C > 0$ for all constriction ratios. However, mixed results emerge for solutions with $\theta_{\text{PTFE}} < 90^\circ$. From this plot, we see that the maximum P_C values for solutions with contact angles slightly lower than 90° start negative but eventually cross the zero capillary pressure line. These results support the previously validated observation that positive pressure differentials ($P_L - P_G > 0$) are sometimes required to fill constricted ($d_{\min}/d_{\max} < 1$), hydrophilic pores.⁶³ Through this simple analysis, we can see the inherently protective effect of constricted pore geometry with regards to electrode flooding. Considering this possibility, we suggest that porous media be selected according to specifics of the pore geometry (i.e., packed particles or

fibers) in addition to other factors (average pore diameter, thickness, etc.). However, we cannot neglect the fact that adding constrictions to the porous substrate (i.e., decreasing d_{\min}/d_{\max}) could negatively impact other transport phenomena in the GDE (e.g., gas phase diffusion) by way of increasing the tortuosity and/or decreasing overall permeability,⁶⁶ although the magnitude of the extent of this tradeoff has yet to be determined in this context.

Opportunities for the integration of oleophobic materials

Oleophobic treatments constitute a readily-available modification to GDEs that may better suit aqueous-organic environments.³¹ Introducing oleophobicity to PTFE sheets has enabled their use as venting materials in electronic devices such as in batteries and other electronics filled with organic solvents.⁶⁷ Although measuring the intrinsic wettability of rough or porous materials with macroscopic sessile drop methods, we can still compare the relative effectiveness of modifying the PTFE surface. Using the same methods as described before for solid PTFE (*vide supra*), we measured the apparent contact angles (**Figure 8**) of the test liquids on two different porous sheets, expanded PTFE (PM21M, Porex) and sintered oleophobic PTFE (PMV15T, Porex) sheets. The raw data are reported in **Tables S6** and **S7** of the Supplementary Information. The non-wetting envelope ($\theta > 90^\circ$) for all of the test liquids is expanded for the porous materials as compared to the dense, flat PTFE sheet shown in **Figure 1**. As mentioned earlier, surface roughness and entrapped gases can increase the apparent phobicity/philicity of a given solid-liquid combination. However, while the porous PTFE membrane is ultimately wetted by lower surface tension mixtures, the oleophobic membrane does not exhibit any $\theta < 90^\circ$. These initial results demonstrate that appropriate modifications to extant and proven material sets may greatly improve the wettability characteristics. While the oleophobic treatment here was applied to a PTFE substrate, in principle, it could be expanded to other polymers, metals, or carbon substrates to improve liquid repellency or tune wettability.

Conclusions and Outlook

The generation of concentrated liquid products at CO₂ electrolyzer outlets is an economically attractive operating objective (*vide supra*) that may be attainable by targeting high current to liquid sweep rate ratios. Investigating these conditions using a simple mass balance model, in combination with *ex situ* contact angle measurements, enables simulation of the local environment at the cathode-electrolyte interface and the propensity of GDE flooding due to enrichment by organic products. Such critical compositions are illustrated in contour plots enabling connections between cell operating conditions (liquid sweep rate and applied currents) and electrode properties (wettability). Such estimations of electrode flooding enable us to predict that FA-generating electrolyzers should be more stable than the equivalent alcohol-producing electrolyzers when targeting high-mass-fraction effluents. We observe that

it may be possible to exploit the complex imbibition behavior of realistic microstructures towards engineering robust GDEs. We also see an opportunity to leverage existing knowledge about surface modification technologies to augment the wettability characteristics of current GDE material sets, possibly with oleophobic treatments, with the goal of expanding the stable operating envelope for CO₂-to-alcohols electrolyzers. Through this exploration of some of the material challenges that face CO₂R during the necessary scale-up phase, we hope to inspire additional researchers in this field to consider these obstacles at an early stage of technology development.

Conflict of Interest

We wish to confirm that there are no known conflicts of interest associated with this publication and there has been no significant financial support for this work that could have influenced its outcome.

CRedit author statement

McLain E. Leonard: Conceptualization, Methodology, Formal Analysis, Investigation, Resources, Writing – Original Draft, Writing – Review & Editing, Visualization **Michael J. Orella:** Methodology, Software, Writing – Original Draft, Writing – Review & Editing **Nick Aiello:** Investigation **Yuriy Román-Leshkov:** Supervision **Antoni Forner-Cuenca** Methodology, Formal Analysis, Writing – Review & Editing **Fikile R. Brushett:** Funding Acquisition, Project Administration, Supervision, Writing – Review & Editing

Acknowledgments

The authors acknowledge the financial support of DOE SBIR Contract #DE-SC0015173. The authors kindly thank the members of the Gleason Group and Prof. Karen Gleason for supporting us as we used their goniometer system to measure contact angles. The authors also thank Lauren E. Clarke and Charles T.-C. Wan of the Brushett Research Group for insightful discussions.

List of Symbols

Variable	Unit	Description
d_{\max}	m	maximum pore diameter
d_{\min}	m	minimum pore diameter
I	A	current
\dot{m}_{out}	kg s ⁻¹	total mass flow rate exiting the reactor
$\dot{m}_{\text{P,in}}$	kg s ⁻¹	product feed rate
$\dot{m}_{\text{w,in}}$	kg s ⁻¹	water feed rate
$\dot{m}_{\text{P,rxn}}$	kg s ⁻¹	product generation rate

$m_{W,rxn}$	kg s ⁻¹	water consumption rate
P_C	bar	capillary pressure
P_G	bar	gas phase pressure
P_L	bar	liquid phase pressure
Q	mL min ⁻¹	volumetric flow rate of feed water
r	m	cylindrical pore radius
x_P	-	mass fraction of product
x_W	-	mass fraction of water
z	m	longitudinal cylindrical coordinate

Constant	Value		Unit	Description
F	96485		C mol e ⁻¹	Faraday constant
M_P	FA	0.04603	kg mol ⁻¹	molar mass of a CO2R product
	MeOH	0.03204		
	EtOH	0.04607		
	PrOH	0.06009		
M_W	0.01802		kg mol ⁻¹	molar mass of water
n_P	(Table 1)		mol CO ₂ mol P ⁻¹	carbon ratio
z_P			mol e mol P ⁻¹	electron-product ratio
z_W			mol e mol W ⁻¹	electron-water ratio
ρ_W	998.2071		kg m ⁻³	density of water at STP
Greek letter			Unit	Description
α			°	filling angle
γ			mN m ⁻¹	liquid-gas surface tension
γ_{C0}			mN m ⁻¹	critical surface tension for complete wetting ($\theta = 0^\circ$)
γ_{C90}			mN m ⁻¹	crossover surface tension ($\theta = 90^\circ$)
θ			°	solid-liquid-gas contact angle

References

1. W. A. Smith, T. Burdyny, D. A. Vermaas, and H. Geerlings, *Joule*, **3**, 1822–1834 (2019).
2. R. M. Darling, K. G. Gallagher, J. A. Kowalski, S. Ha, and F. R. Brushett, *Energy Environ. Sci.*, **7**, 3459–3477 (2014).
3. P. D. Luna, C. Hahn, D. Higgins, S. A. Jaffer, T. F. Jaramillo, and E. H. Sargent, *Science*, **364**, eaav3506 (2019).
4. Y. Hori, in *Modern aspects of electrochemistry*, p. 89–189, Springer (2008) http://link.springer.com/chapter/10.1007/978-0-387-49489-0_3.

5. J. T. Feaster, C. Shi, E. R. Cave, T. Hatsukade, D. N. Abram, K. P. Kuhl, C. Hahn, J. K. Nørskov, and T. F. Jaramillo, *ACS Catal.*, 4822–4827 (2017).
6. S. Ringe, E. L. Clark, J. Resasco, A. Walton, B. Seger, A. T. Bell, and K. Chan, *Energy Environ. Sci.* (2019) <https://pubs.rsc.org/en/content/articlelanding/2019/ee/c9ee01341e>.
7. P. Lobaccaro, M. R. Singh, E. L. Clark, Y. Kwon, A. T. Bell, and J. W. Ager, *Phys. Chem. Chem. Phys.*, **18**, 26777–26785 (2016).
8. L.-C. Weng, A. T. Bell, and A. Z. Weber, *Phys. Chem. Chem. Phys.*, **20**, 16973–16984 (2018).
9. T. Burdyny and W. A. Smith, *Energy Environ. Sci.*, **12**, 1442–1453 (2019).
10. M. R. Thorson, K. I. Siil, and P. J. A. Kenis, *J. Electrochem. Soc.*, **160**, F69–F74 (2013).
11. B. Kim, F. Hillman, M. Ariyoshi, S. Fujikawa, and P. J. A. Kenis, *Journal of Power Sources*, **312**, 192–198 (2016).
12. C. Chen, J. F. Khosrowabadi Kotyk, and S. W. Sheehan, *Chem*, **4**, 2571–2586 (2018).
13. G. O. Larrazábal, P. Strøm-Hansen, J. P. Heli, K. Zeiter, K. T. Therkildsen, I. Chorkendorff, and B. Seger, *ACS Appl. Mater. Interfaces*, **11**, 41281–41288 (2019).
14. Z. Yin, H. Peng, X. Wei, H. Zhou, J. Gong, M. Huai, L. Xiao, G. Wang, J. Lu, and L. Zhuang, *Energy Environ. Sci.*, **12**, 2455–2462 (2019).
15. Z. Liu, H. Yang, R. Kutz, and R. I. Masel, *Journal of The Electrochemical Society*, **165**, J3371–J3377 (2018).
16. H. S. Fogler, *Elements of Chemical Reaction Engineering*, 4th ed., p. 1081, Prentice Hall, (2006).
17. M. J. Orella, S. M. Brown, M. E. Leonard, Y. Román-Leshkov, and F. R. Brushett, *Energy Technology*, **n/a**, 1900994.
18. F. P. G. de Arquer, C.-T. Dinh, A. Ozden, J. Wicks, C. McCallum, A. R. Kirmani, D.-H. Nam, C. Gabardo, A. Seifitokaldani, X. Wang, Y. C. Li, F. Li, J. Edwards, L. J. Richter, S. J. Thorpe, D. Sinton, and E. H. Sargent, *Science*, **367**, 661–666 (2020).
19. B. Endrődi, E. Kecsenvity, A. Samu, F. Darvas, R. V. Jones, V. Török, A. Danyi, and C. Janáky, *ACS Energy Lett.*, **4**, 1770–1777 (2019).
20. H. Yang, J. J. Kaczur, S. D. Sajjad, and R. I. Masel, *Journal of CO2 Utilization*, **20**, 208–217 (2017).
21. C. M. Gabardo, C. P. O'Brien, J. P. Edwards, C. McCallum, Y. Xu, C.-T. Dinh, J. Li, E. H. Sargent, and D. Sinton, *Joule* (2019) <http://www.sciencedirect.com/science/article/pii/S2542435119303654>.

22. D. S. Ripatti, T. R. Veltman, and M. W. Kanan, *Joule*, **3**, 240–256 (2019).
23. C.-T. Dinh, F. P. García de Arquer, D. Sinton, and E. H. Sargent, *ACS Energy Lett.*, **3**, 2835–2840 (2018).
24. C.-T. Dinh, T. Burdyny, M. G. Kibria, A. Seifitokaldani, C. M. Gabardo, F. P. G. de Arquer, A. Kiani, J. P. Edwards, P. D. Luna, O. S. Bushuyev, C. Zou, R. Quintero-Bermudez, Y. Pang, D. Sinton, and E. H. Sargent, *Science*, **360**, 783–787 (2018).
25. W. Vielstich, A. Lamm, and H. A. Gasteiger, Eds., *Handbook of Fuel Cells : Fundamentals, Technology, and Applications*, Wiley, (2003) <https://lib.mit.edu/record/cat00916a/mit.001126960>.
26. S. Pinnow, N. Chavan, and T. Turek, *J Appl Electrochem*, **41**, 1053–1064 (2011).
27. T. Haas, R. Krause, R. Weber, M. Demler, and G. Schmid, *Nature Catalysis*, **1**, 32–39 (2018).
28. E. W. Washburn, *Phys. Rev.*, **17**, 273–283 (1921).
29. W. M. Deen, *Analysis of Transport Phenomena*, 2nd ed., p. 688, Oxford University Press, (2011).
30. P.-G. de Gennes, F. Brochard-Wyart, and D. Quéré, *Capillarity and Wetting Phenomena: Drops, Bubbles, Pearls, Waves*, p. 291, Springer, New York, NY, (2010).
31. W. A. Zisman, in *Contact Angle, Wettability, and Adhesion*, Advances in Chemistry., vol. 43, p. 1–51, AMERICAN CHEMICAL SOCIETY (1964) <https://doi.org/10.1021/ba-1964-0043.ch001>.
32. P. M. Dunlap and S. R. Faris, *Nature*, **196**, 1312–1313 (1962).
33. P. K. Weissenborn and R. J. Pugh, *Journal of Colloid and Interface Science*, **184**, 550–563 (1996).
34. E. Álvarez, G. Vázquez, M. Sánchez-Vilas, B. Sanjurjo, and J. M. Navaza, *Journal of Chemical & Engineering Data*, **42**, 957–960 (1997).
35. Z.-B. Li, Y.-G. Li, and J.-F. Lu, *Ind. Eng. Chem. Res.*, **38**, 1133–1139 (1999).
36. H. Ohshima and H. Matsubara, *Colloid Polym Sci*, **282**, 1044–1048 (2004).
37. T. Young, *Phil. Trans. R. Soc. Lond.*, **95**, 65–87 (1805).
38. R. N. Wenzel, *Ind. Eng. Chem.*, **28**, 988–994 (1936).
39. A. B. D. Cassie and S. Baxter, *Transactions of the Faraday Society*, **40**, 546 (1944).

40. ISO 4920:2012, *Textile fabrics — Determination of resistance to surface wetting (spray test)*, International Organization for Standardization, Geneva, Switzerland, (2012) <https://www.iso.org/standard/50706.html>.
41. ISO 9073-17:2008, *Textiles — Test methods for nonwovens — Part 17: Determination of water penetration (spray impact)*, International Organization for Standardization, Geneva, Switzerland, (2008) <https://www.iso.org/standard/42095.html>.
42. C. Xia, P. Zhu, Q. Jiang, Y. Pan, W. Liang, E. Stavitski, H. N. Alshareef, and H. Wang, *Nature Energy*, **4**, 776–785 (2019).
43. M. J. Orella, *DropPy*, (2020) <https://github.com/michaelorella/droppy>.
44. J. R. Rumble, Ed., *CRC Handbook of Chemistry and Physics*, 99th Edition., CRC Press/Taylor & Francis, Boca Raton, FL, (2018).
45. A. Kozbial, C. Trouba, H. Liu, and L. Li, *Langmuir*, **33**, 959–967 (2017).
46. C. Delacourt, P. L. Ridgway, J. B. Kerr, and J. Newman, *Journal of The Electrochemical Society*, **155**, B42 (2008).
47. M. S. Naughton, F. R. Brushett, and P. J. A. Kenis, *Journal of Power Sources*, **196**, 1762–1768 (2011).
48. F. R. Brushett, M. S. Naughton, J. W. D. Ng, L. Yin, and P. J. A. Kenis, *International Journal of Hydrogen Energy*, **37**, 2559–2570 (2012).
49. M. S. Naughton, G. H. Gu, A. A. Moradia, and P. J. A. Kenis, *Journal of Power Sources*, **242**, 581–588 (2013).
50. K. Wu, E. Birgersson, B. Kim, P. J. A. Kenis, and I. A. Karimi, *J. Electrochem. Soc.*, **162**, F23–F32 (2015).
51. S. Verma, X. Lu, S. Ma, R. I. Masel, and P. J. A. Kenis, *Phys. Chem. Chem. Phys.*, **18**, 7075–7084 (2016).
52. B. Kim, F. Hillman, M. Ariyoshi, S. Fujikawa, and P. J. A. Kenis, *Journal of Power Sources*, **312**, 192–198 (2016).
53. S. Verma, Y. Hamasaki, C. Kim, W. Huang, S. Lu, H.-R. M. Jhong, A. A. Gewirth, T. Fujigaya, N. Nakashima, and P. J. A. Kenis, *ACS Energy Lett.*, **3**, 193–198 (2018).
54. K. Liu, W. A. Smith, and T. Burdyny, *ACS Energy Lett.*, 639–643 (2019).
55. C. M. Gabardo, A. Seifitokaldani, J. P. Edwards, C.-T. Dinh, T. Burdyny, M. G. Kibria, C. P. O'Brien, E. H. Sargent, and D. Sinton, *Energy Environ. Sci.*, **11**, 2531–2539 (2018).
56. D. Salvatore and C. P. Berlinguette, *ACS Energy Lett.*, 215–220 (2019).

57. Y. Xu, J. P. Edwards, J. Zhong, C. P. O'Brien, C. M. Gabardo, C. McCallum, J. Li, C.-T. Dinh, E. H. Sargent, and D. Sinton, *Energy Environ. Sci.* (2019) <https://pubs.rsc.org/en/content/articlelanding/2020/ee/c9ee03077h>.
58. J. P. Edwards, Y. Xu, C. M. Gabardo, C.-T. Dinh, J. Li, Z. Qi, A. Ozden, E. H. Sargent, and D. Sinton, *Applied Energy*, **261**, 114305 (2020).
59. K. G. Schulz, U. Riebesell, B. Rost, S. Thoms, and R. E. Zeebe, *Marine Chemistry*, **100**, 53–65 (2006).
60. A. Kutana and K. P. Giapis, *Nano Lett.*, **6**, 656–661 (2006).
61. D. J. Lomax, P. Kant, A. T. Williams, H. V. Patten, Y. Zou, A. Juel, and R. A. W. Dryfe, *Soft Matter*, **12**, 8798–8804 (2016).
62. W. R. Purcell, *Journal of Petroleum Technology*, **2**, 11–12 (1950).
63. A. Forner-Cuenca, J. Biesdorf, A. Lamibrac, V. Manzi-Orezzoli, F. N. Büchi, L. Gubler, T. J. Schmidt, and P. Boillat, *Journal of The Electrochemical Society*, **163**, F1038–F1048 (2016).
64. J. T. Gostick, M. A. Ioannidis, M. W. Fowler, and M. D. Pritzker, *Journal of Power Sources*, **194**, 433–444 (2009).
65. G. Mason and N. R. Morrow, *Journal of Colloid and Interface Science*, **168**, 130–141 (1994).
66. J. T. Gostick, M. W. Fowler, M. D. Pritzker, M. A. Ioannidis, and L. M. Behra, *Journal of Power Sources*, **162**, 228–238 (2006).
67. Porex <https://www.porex.com/markets/electronics/ip-rated-protection-vents/>.

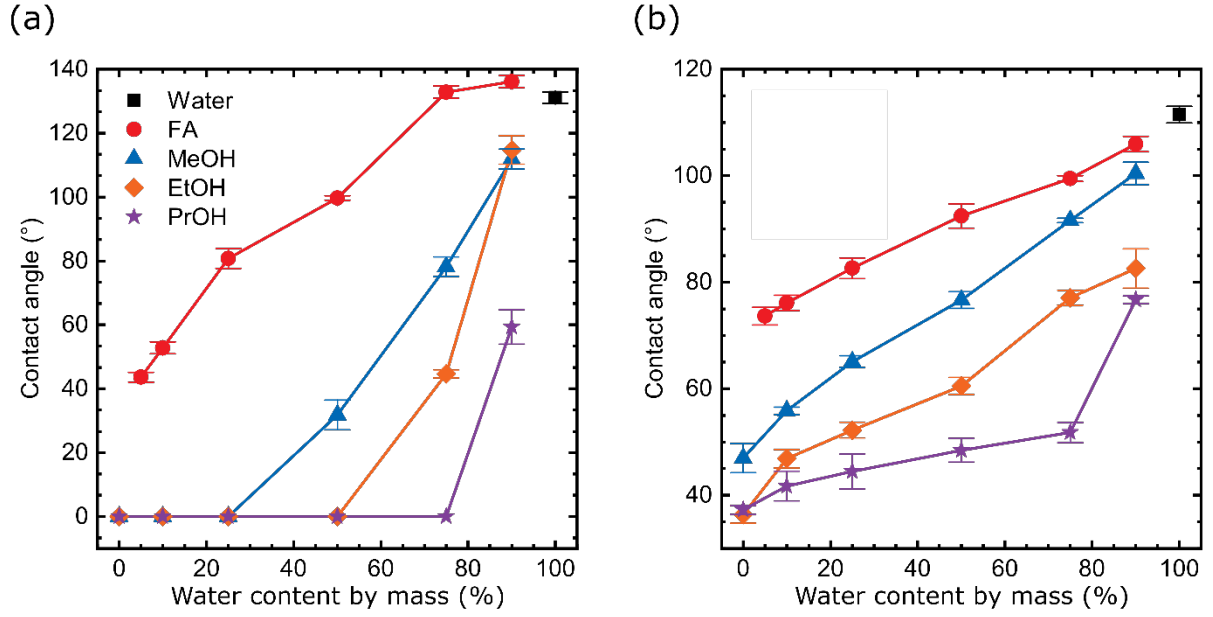


Figure 1. Sessile drop contact angles on (a) graphite and (b) PTFE for an array of liquid CO₂R products as a function of water content by mass.

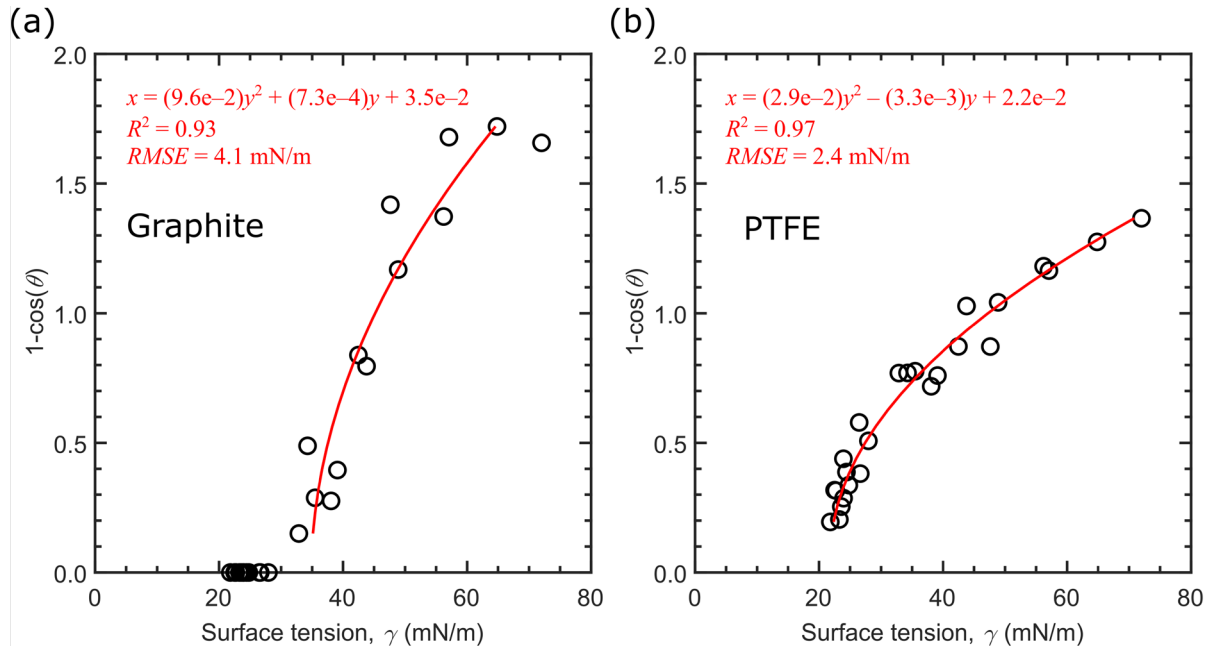


Figure 2. Zisman plots for (a) graphite and (b) PTFE with all the CO₂R test liquids are used to predict wettability with surface tension, γ , as a common descriptor. Empirical quadratic fits ($x = \gamma$, $y = 1-\cos(\theta)$) are plotted in red and are used for determining critical surface tensions, such as γ_{C0} and γ_{C90} , associated with each material.

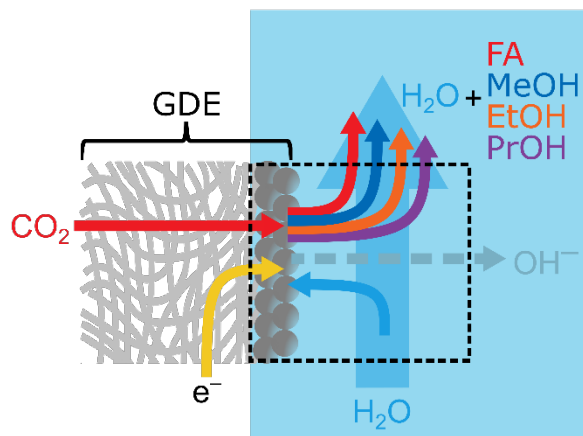


Figure 3. Electrolyzer mass balance model schematic. Water is fed to the cathode GDE where CO_2 , water (H_2O), and electrons (e^-) are consumed within the catalyst layer to produce liquid organic components. The exiting stream contains an aqueous-organic mixture. We do not include the contributions of hydroxide (OH^-) ions and other anions on the overall mass balance or liquid phase properties.

Table 1. CO_2R half-reaction stoichiometry for liquid products

Half reaction	n_{P} (mol CO_2 /mol P)	z_{P} (mol e ⁻ /mol P)	z_{W} (mol e ⁻ /mol W)	M_{P} (g/mol P)
$\text{CO}_2 + 2\text{e}^- + \text{H}_2\text{O} \rightarrow \text{HCOO}^- + \text{OH}^-$	1	2	2	46.03
$\text{CO}_2 + 6\text{e}^- + 5\text{H}_2\text{O} \rightarrow \text{CH}_3\text{OH} + 6\text{OH}^-$	1	6	6/5	32.04
$2\text{CO}_2 + 12\text{e}^- + 9\text{H}_2\text{O} \rightarrow \text{C}_2\text{H}_5\text{OH} + 12\text{OH}^-$	2	12	12/9	46.07
$3\text{CO}_2 + 18\text{e}^- + 13\text{H}_2\text{O} \rightarrow \text{C}_3\text{H}_7\text{OH} + 18\text{OH}^-$	3	18	18/13	60.09

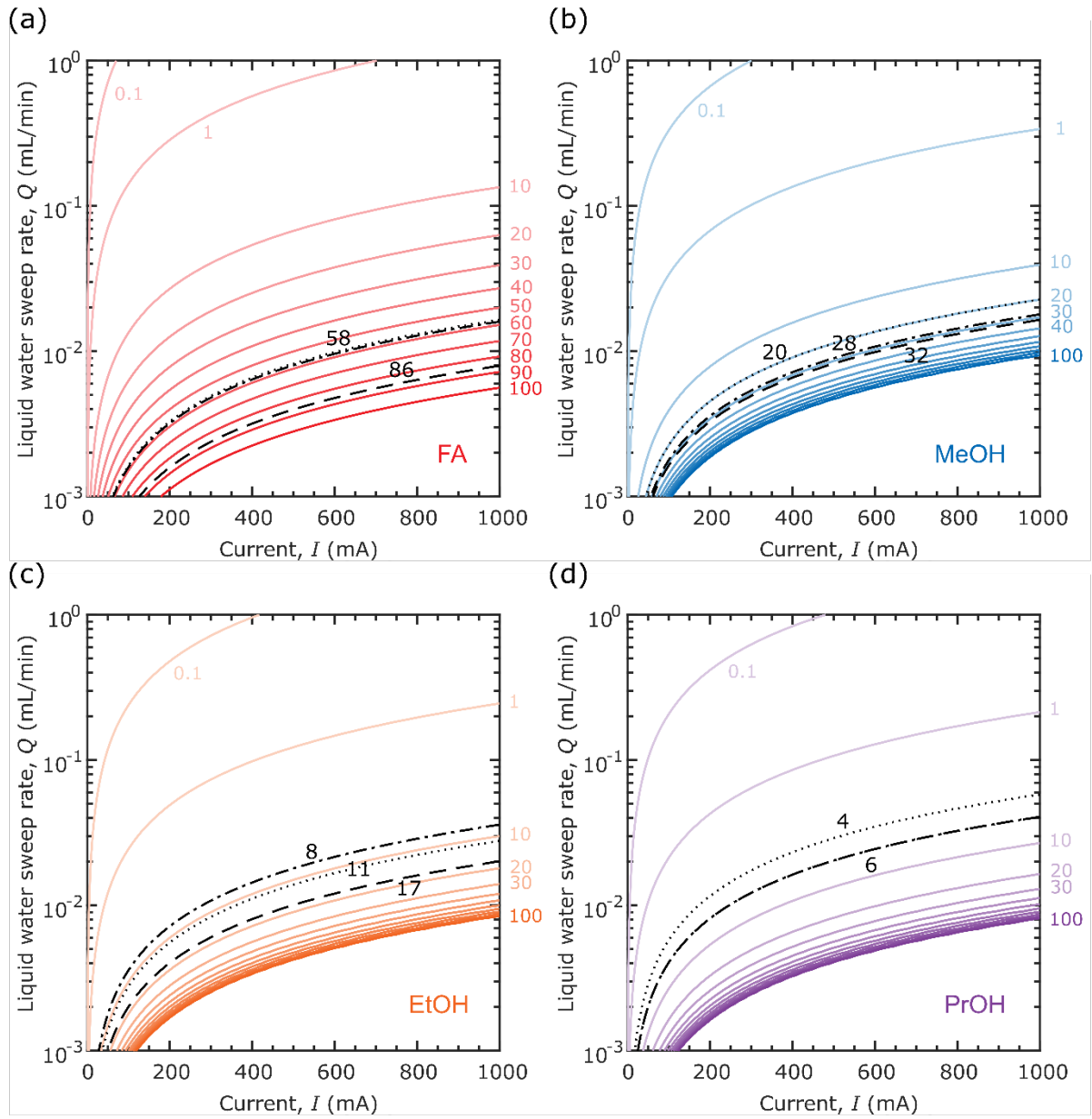


Figure 4. The liquid product concentration, x_P , reported in product content by mass (%) with the solid contours, is calculated for (a) FA, (b) MeOH, (c) EtOH, and (d) PrOH as a function of liquid inlet water flow rate and current by using a mass balance around a hypothetical CO_2 electrolyzer with a flowing electrolyte stream. The additional black dashed lines correspond to the measured (·-) and theoretically predicted (···, 47 mN/m from this work; ---, 40 mN/m from Zisman) $\theta = 90^\circ$ point on PTFE at which the mixture transitions from non-wetting to wetting.

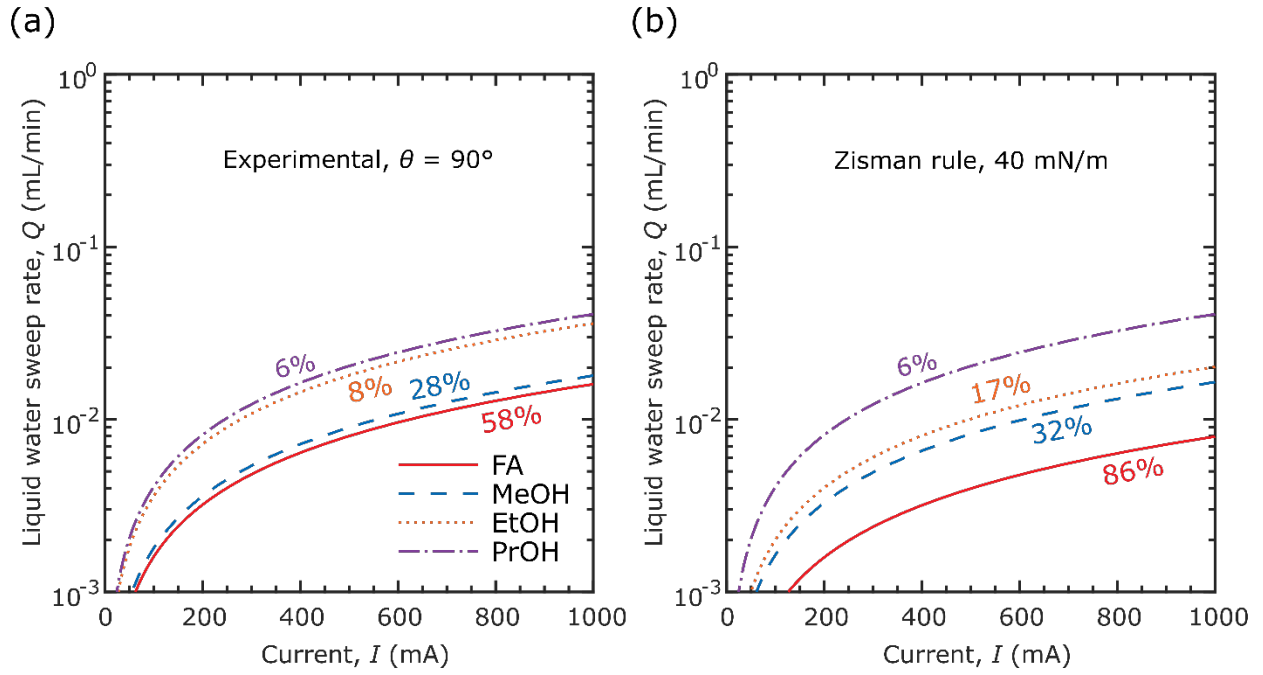


Figure 5. Crossover composition contours correspond to $\theta = 90^\circ$ on PTFE (when $P_C = 0$ bar) as (a) measured in this work and (b) predicted from a Zisman rule surface tension threshold ($\theta = 90^\circ$) of 40 mN/m for nonpolar solvents on PTFE.

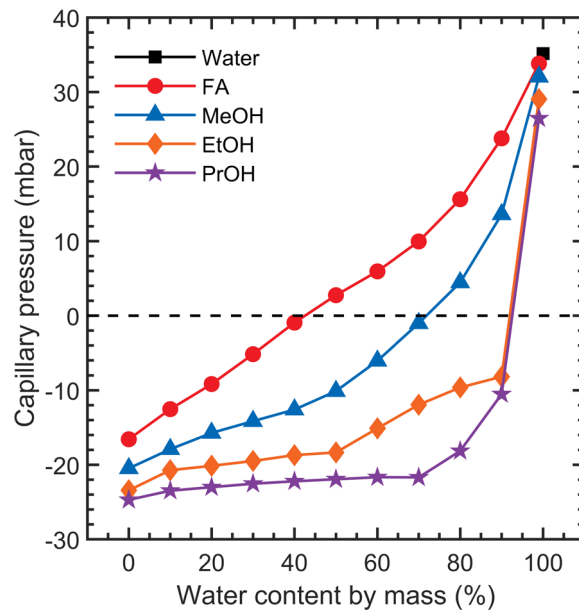


Figure 6. Capillary pressure, P_C , is calculated as a function of water content by mass, x_w , and CO₂R liquid product for a cylindrical pore diameter of 30 μm .

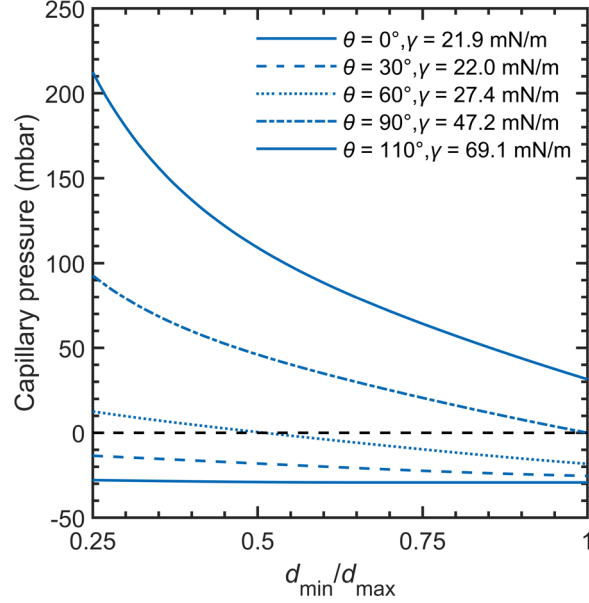


Figure 7. Maximum capillary pressure is calculated for a constricted cylindrical pore ($d_{\max} = 30 \mu\text{m}$) as a function of the ratio between minimum and maximum pore diameters, d_{\min}/d_{\max} . The contour lines correspond to different combinations of (γ, θ) for a generalized liquid CO2R product on PTFE as defined by the (red) Zisman plot polynomial fit line shown in **Figure 2b**. By adding a constriction ($d_{\min}/d_{\max} < 1$) to an otherwise cylindrical channel, we see that a positive pressure difference is required to flood the pore for liquid mixtures with $\theta < 90^\circ$.

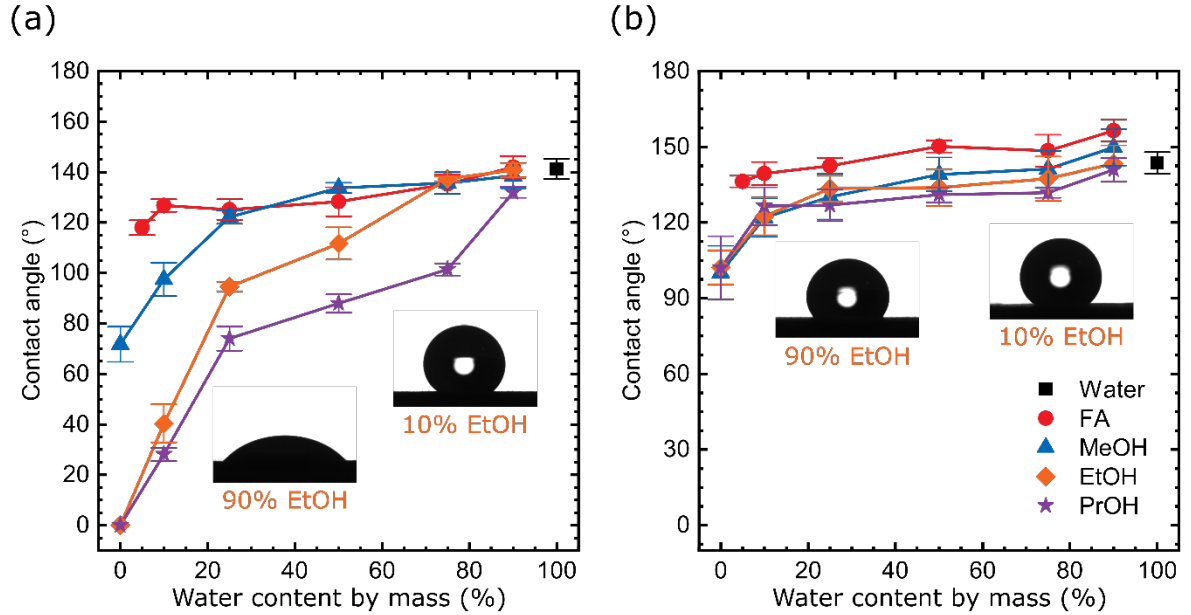


Figure 8. Apparent sessile drop contact angles for selected CO2R product liquids as a function of water content by mass on (a) Porex PM21M expanded PTFE and (b) Porex PMV15T oleophobic treated sintered PTFE sheet.